Local Based Calibration of the Thermoelastic Signal using Thermoelastic Stress Analysis and Digital Image Correlation

Francisco de Sá Rodrigues
francisco.sa.rodrigues@tecnico.ulisboa.pt

Instituto Superior Técnico, Universidade de Lisboa, Portugal

November 2019

Abstract

Presently, the usage of Thermoelastic Stress Analysis (TSA) implies the pre-determination of some thermo-mechanical properties and the assumption of a model that best characterizes the material's global thermoelastic behaviour. However, due to the inherent heterogeneity of composite materials, these assumptions prove to under/overestimate the stress/strain magnitude. This work aims to correct the assumption that the material's thermoelastic response is a global behaviour instead of a local one, since it depends of characteristics such as, the thickness of the resin rich layer, presence of voids and stacking sequence. Therefore, Digital Image Correlation (DIC) will be used to compute the strain fields in Carbon Fiber Reinforced Polymers (CFRP) which will be converted into thermal amplitude through the thermoelastic equations, already proposed in the literature, and compared with the results obtained through the infrared (IR) camera. These results will be replicated for several stacking sequences and a point-wise map with the thermoelastic models will be presented.
Keywords: Thermoelastic Stress Analysis, Digital Image Correlation, Carbon Fiber Reinforced Polymers, Structural Health Monitoring, Local Thermoelastic Calibration

1. Introduction

Fiber-reinforced polymers (FRPs), like Carbon and Glass fiber-reinforced polymers (CFRP and GFRP, respectively) have been gaining increasing usage in the aerospace industry due to the superior strength-to-weight ratios presented by these materials, while delivering a higher corrosion and fatigue resistance in comparison to metals, like Aluminium alloys. Furthermore, the incorporation of this type of materials in the manufacture of aircraft structures also enabled a higher complexity and aerodynamic optimization [1] due to its ability to assume more complex shape. Whilst metals, due to their manufacturing limitations, do not present such qualities. These materials are being employed in structures of the aircrafts where high loads and frequency levels need to be withstood [2].

In the aerospace industry, the continuous usage of a structure, in operational cycles, leads to the reduction of its lifetime for which preventive maintenance is currently being employed based in non-destructive inspections (NDI) [3]. Addressing this issue, several SHM techniques have been proposed for the in-operation assessment of the material's stress/strain fields. Proposals consist in the employment of complex systems capable of acquiring data continuously and provide quantitative damage evaluation.

Of the several researched SHM techniques, Thermoelastic Stress Analysis (TSA) [4] and Digital Image Correlation (DIC) [5] have stood out for their non-destructive, non-contact characteristic while providing continuous full-field stress/strain measurement of the material, during operations.

TSA refers to the experimental technique which relies on the measurement of the thermoelastic phenomenon that occurs in solids when subjected to cyclic tensile/compressive loads under adiabatic and reversible conditions (isentropic conditions). These conditions can be achieved if the stress induced during cyclic loading is inferior to the yield stress, meaning the material is in the linear elastic region.

However, current TSA measurements resort to a global calibration of the thermoelastic signal through employment of strain gauges or extensometers during cyclic load test. These measurement systems provide an average value for the laminate's strain change during the loading limits of

the sample. These values, considered the theoretical results, are converted into temperature change values by replacing them in the thermoelastic models' equations. Afterwards, these theoretical values are compared with the values obtained from the infrared camera output signal. The model which will be selected to characterize the behaviour of the whole system corresponds to the one that gives the lowest error.

The previous methodology does not fully take advantage of the TSA's full-field advantages since the global calibration of the material assumes an homogeneity in the material. In materials such as FRPs, this assumption proves to under/overestimate the mechanical deformation in critical regions that might lead to safety issues in the aerospace industry.

Therefore, by employing DIC in material deformation measurements a local-based evaluation of the material's strain is obtained. Incorporation of point-wise strain values in the thermoelastic model equations allows the comparison between two local-based approaches generates a solution which takes into account locations with different thermoelastic responses. This constitutes the main objective for this work.

2. Digital Image Correlation (DIC)

DIC is a SHM technique which allows the acquisition, storage and analysis of a set of images from an object, through the employment of CCD/CMOS sensors in digital cameras, in order to obtain a full field evaluation of material's displacement. Motion estimation is done by monitoring and identifying changes in the surface pattern through the comparison of the acquired images with a reference stage (typically an unloaded configuration). For this, the system assumes continuity is present in the sample's surface, meaning the differences detected in the sensor's plane also occur in the object. Therefore, the surface should present, or be painted with, a gray distribution pattern, usually referred to as speckle pattern.

Perfectly adiabatic thermoelastic effects are characterized by in-plane motions which makes through-thickness motion evaluation (3D DIC) redundant for the present work. This leads to one big advantage regarding system's calibration, since this procedure was experienced to be much simpler for only one camera. Moreover, the employment of two cameras makes the system highly sensitive to the camera's motion, since a "yaw" angle is required, for each cameras.

Subsequently, in-plane deformations are monitored with the sensor's axis perpendicular to the sample's surface, providing plane stress conditions are valid and no sudden change of lightning occurs, which might lead to inaccurate subset matching. Image correlation is performed by quantifying the intensity signal of the gray distribution, based on a gradient ranging from black to white, given in accordance to the number of bits available in the sensor. Subset (squared sensor area composed by a given number of pixels) matching is performed by evaluating a given region of interest (ROI) of the acquired images, prior and after deformation, through a correlation function. The correlation function incorporated for image matching is denominated, the Normalized Cross Correlation [6], which yields,

$$C(x,y) = 1 - \sum_{i=1}^{N}\sum_{j=1}^{M} \frac{I(x_i,y_j)I'(x'_i,y'_i))}{I^2(x_i,y_j)I'^2(x'_i,y'_i)^{\frac{1}{2}}} \quad (1)$$

$$x'_i = x_i + u_i(x_i,y_j)$$
$$y'_i = y_j + v_i(x_i,y_j)$$

where I and I' represent the continuously interpolated discrete intensity pattern value given prior and after deformation, respectively, at a given location in the sensor's plane; x'_i and y'_i are the location of the subset's center after deformation and, $u_i(x_i,y_j)$ and $v_i(x_i,y_j)$, the displacement of this point. This displacement can be estimated through different order shape functions (i.e, for this work a second order shape function was used). An ideal subset matching (figure 1) is given by the minimization of the function in equation 1.

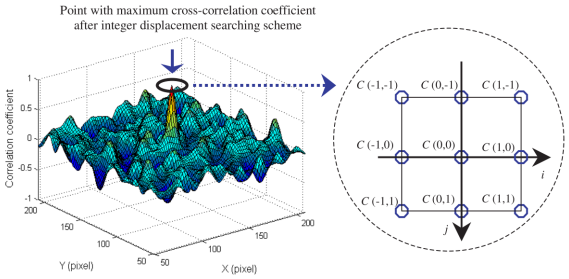

Figure 1: Subset Matching[7]

In the subset's deformed configuration, some of the subset's coordinates might be located between pixels. The locations for these points should be computed to obtain more accurate image correlation. However, all the aforementioned methods evaluate the intensity of the signal in a pixel-wise manner, which implies that the DIC system must transform the discrete intensity values, in the sensor plane I(i,j), into a continuous map by employing an interpolation function. For the present work, the bi-cubic spline interpolation was used, since it gives the most accurate measurements[7].

Introduction of sub-pixel accuracy for the displacement measurements requires two consecutive steps[7]: initial deformation estimation and

sub-pixel displacement measurements. For this, the Newton Raphson iterative spatial cross-correlation algorithm is usually employed. According to this method, the calculation path is defined by the ROI and subset correspondence will be sought within its boundaries. For improvement of the computation time, displacement estimations in the current point are assumed to be equivalent to the next points value. Classic algorithm incorporated in most DIC systems for in-plane displacement measurement yields,

$$\boldsymbol{p} = \boldsymbol{p}_0 - \frac{\nabla C(\boldsymbol{p}_0)}{\nabla\nabla C(\boldsymbol{p}_0)} \tag{3}$$

where $\mathbf{p_0}$ is the initial guess of the solution, $\mathbf{p}$ is the next iterative solution, $\nabla C(\mathbf{p_0})$ is the gradients of the correlation function and $\nabla\nabla C(\mathbf{p_0})$ is the Hessian matrix of the correlation function.

3. Thermoelastic Stress Analysis (TSA)

The mathematical expression describing the thermoelastic phenomenon was firstly developed by Thomson[8], relying on the first and second law of thermodynamics and classical mechanics. This formulation relates the material's isentropic temperature change (ΔT), with the first stress invariant change($\Delta\sigma_i$), in solid isotropic materials

$$\frac{\Delta T}{T_0} = -\frac{\alpha}{\rho C_p}\Delta(\sigma_1 + \sigma_2) \tag{4}$$

where ρ is the material's density, α is the coefficient of thermal expansion (CTE), T_0 the absolute temperature and C_p the specific heat coefficient, at constant pressure.

This equation was later on extended to consider orthotropic materials, such as composite materials, for which the temperature is a linear combination of the material's CTE and the stress change, in the principal directions

$$\frac{\Delta T}{T_0} = -\frac{1}{\rho C_p}[\alpha]^T_{1,2}[\Delta\sigma]_{1,2} \tag{5}$$

Strain data is attained through employment of strain gauges or extensometers. Therefore, switching from a stress to a strain dependent equation simplifies quantitative TSA work. Moreover, in composite materials with multi-directional stacking sequences subjected to in-plane loading, the applied strain/load can be assumed equal throughout the laminate, whilst the generated stress will vary according to the ply's fiber direction [9].

$$\frac{\Delta T}{T_0} = -\frac{T_0}{\rho C_p}[\alpha]^T_{1,2}[Q]_{1,2}[\Delta\epsilon]_{1,2} \tag{6}$$

Strain values obtained with the previously mentioned devices are given in the loading system of axes (x,y) which might not correspond to the surface lamina's principle direction (1,2). Therefore, by employing transformation matrices, where θ is given by the angle of the fibers, equation 7 assumes the classical formulation for TSA, in orthotropic materials

$$\frac{\Delta T}{T_0} = -\frac{1}{\rho C_p}[\alpha]^T_{1,2}[Q]_{1,2}[T]_\epsilon[\Delta\epsilon]_{x,y} \tag{7}$$

where $[Q]_{1,2}$ is the reduced stiffness matrix and $[T]_\epsilon$ is the transformation matrix for strain terms,

$$\begin{bmatrix}\sigma_1\\ \sigma_2\\ \tau_6\end{bmatrix} = \begin{bmatrix}Q_{11} & Q_{12} & 0\\ Q_{21} & Q_{22} & 0\\ 0 & 0 & Q_{66}\end{bmatrix}\begin{bmatrix}\epsilon_{11}\\ \epsilon_{22}\\ \gamma_{66}\end{bmatrix} \tag{8}$$

$$\begin{bmatrix}\epsilon_{11}\\ \epsilon_{22}\\ \gamma_{66}\end{bmatrix} = \begin{bmatrix}c^2 & s^2 & cs\\ s^2 & c^2 & -cs\\ -2cs & 2cs & c^2-s^2\end{bmatrix}\begin{bmatrix}\epsilon_x\\ \epsilon_y\\ \gamma_s\end{bmatrix} \tag{9}$$

furthermore, $c = cos(\theta)$ and $s = sin(\theta)$. For balanced and symmetric laminates, $\gamma_s = 0$. After factorizing equation 7, the following equation is obtained,

$$\frac{\Delta T}{T_0} = -\frac{1}{\rho C_p}[(\alpha_1 Q_{11} + \alpha_2 Q_{12})(\Delta\epsilon_x c^2 + \Delta\epsilon_y s^2 + \gamma_s cs) + (\alpha_1 Q_{12} + \alpha_2 Q_{22})(\Delta\epsilon_x s^2 + \Delta\epsilon_y c^2 - \gamma_s cs)]$$

3.1. Strain based thermoelastic models

3.1.1 Resin Rich Layer

Pitarresi et al.[10] described the influence of the surface resin layer on the thermoelastic response of GFRP laminates. The authors concluded that this material acts as a strain witness for the laminate. Under this assumption, the thermoelastic response can be quantified using the mechanical and thermal properties of the external epoxy layer. Since the mechanical response of the external epoxy layer will be identical to the laminate's,

$$\Delta\epsilon_{xR} = \Delta\epsilon_{xc} \tag{10a}$$

$$\epsilon_{xc} + \epsilon_{yc} = \frac{1-\nu_R}{E_R}(\sigma_{xR} + \sigma_{yR}) \tag{10b}$$

where E is the Young's modulus and ν the Poisson's ratio and the subscripts R and c refer to the resin and composite properties.

$$\frac{\Delta T}{T_0} = -\frac{\alpha_R}{\rho_R C_{pR}}\Big[\frac{E_R}{1-\nu_R}(\Delta\epsilon_{xC} + \Delta\epsilon_{yC})\Big] \tag{11}$$

3.1.2 Orthotropic Surface Layer

This model recovers the formulation obtained by factorizing equation 7. According to this result, the thermal response of the laminate is assumed to

originate in the orthotropic surface ply, which for balanced and symmetric laminate yields,

$$\frac{\Delta T}{T_0} = -\frac{1}{\rho C_p}[(\alpha_1 Q_{11} + \alpha_2 Q_{12})(c^2\Delta\epsilon_x + s^2\Delta\epsilon_y) + (\alpha_1 Q_{12} + \alpha_2 Q_{22})(s^2\Delta\epsilon_x + c^2\Delta\epsilon_y)] \quad (12)$$

3.1.3 Homogeneous Model

The material's thermoelastic response is assumed to be dependent solely of the laminate's extensional stiffness matrix $[A_{i,j}]$ and the global coefficients of thermal expansion, α_x and α_y

$$\frac{\Delta T}{T_0} = -\frac{1}{\rho C_p h}\big[\alpha_{xL}(A_{11} + A_{12})\Delta\epsilon_x + \alpha_{yL}(A_{12} + A_{22})\Delta\epsilon_y\big] \quad (13)$$

4. Sample Preparation and Characterisation

4.1. CFRP Laminate Manufacturing

Composite laminates were assembled through hand lay-up of carbon fiber prepreg laminae with the size of 300×300 mm. These prepregs were supplied by Kordsa Company (with the code **KOM10 T700 12KT UD300 37 600 KOMP**) and composed by T700 unidirectional carbon fibers with a fiber areal of 300g/m^2. The curing of the resin was done in an **MSE Teknoloji LTD** manual hot press with the incorporation of a thermocouple connected to a thermometer, which ensured the proper shadowing of the curing cycle of the resin. Afterwards, cooling of the sample was done in a phased manner, approximately $10°$C every 5 minutes, to ensure no residual stresses would remain in the laminate that might induce errors in the IR camera measurements. Table 1 summarises the laminate type and respective stacking sequences, used in the current work.

Laminate Type	Stacking Sequence	Code
UD	$[0]_8$	UD0
Cross-Ply	$[0/90/90/0]_s$	CP(0/90)
Cross-Ply	$[90/0/0/90]_s$	CP(90/0)
Quasi Isotropic	$[0_2/\text{-}45_2/45_2/90_2]_s$	Q.I(0/45)

Table 1: Manufactured Stacking Sequence

4.2. Material Characterization

For the determination of the longitudinal and transverse modulus, 5 samples were taken from a unidirectional laminate with fibers in the longitudinal direction ($0°$) and five samples with fibers in the transverse direction ($90°$) were cut, according to ASTM D3039/D3039M standards (250x15x2mm and 175x25x1.5 mm, respectively). The unidirectional samples were then bonded with GFRP tabs, with dimensions of 50x15x2 mm, using epoxy Araldite 2011 and left to cure at room temperature for 24 hours. This samples were then tested in an Instron 5983 servo-hydraulic machine according to previously mentioned standard. Determination of Poisson Ratio (ν_{12}) required the attachment of biaxial strain gauges to the sample's back, for transverse strain measurement during tensile loading test. Afterwards, values for ν_{21} were determined through the rule of mixture. Calculation of the laminate's density was done following a hydrostatic weighting technique. For this, 5 samples, with dimensions 25x25x2 mm, were weighted using a **Shimadzu AUX220** scale. Values for Specific Heat Coefficient at constant pressure (C_p) were determined using a Differential Scanning Calorimeter (**Mettler Toledo DSC 3+** model), by following ASTM E1269 – 11. A heat flux calibration was initially done, using a synthetic Sapphire sample, for which an average 8% deviation was obtained in relation to the literature standard values. The calculation of the material's Coefficient of Thermal Expansion in the principal directions was done through a Thermomechanical Analysis method, according to ASTM E831-19, using a **Mettler Toledo TMA/SDTA 1 STARe** System. In order to calculate the constituents volume ratio (indicative of the laminate's quality), a void volume ratio test was performed, following ASTM D3171-15. A summary of the results obtained in these tests is presented in table 2.

Property	CFRP lamina	OM 10 Epoxy
E_1 [GPa]	128.382	-
E_2 [GPa]	8.284	-
G_{12} [GPa]	3.58	-
ν_{12}	0.3	-
ν_{21}	0.019	
ρ [g/cm^3]	1.5163	-
C_p [J/kg.K]	763.632	-
α_1 [μ .K^{-1}]	0.55	-
α_2 [μ .K^{-1}]	27.4	-
E_r[GPa]	-	3.583
μ_r	-	0.39
C_{pr} [J/kg.K]	-	841
ρ_r [g/cm^3]	-	1.142
α_r [μ .K^{-1}]	-	58

Table 2: Mechanical and Thermal Properties of Epoxy resin and CFRP lamina

4.3. Yield Point Calculation

For determining the Yield point of each stacking sequence (presented in table 3), samples from each stacking sequence were cut with in-plane dimensions of 250×25mm and tested in an Instron 8801 servo-hydraulic machine.

Stacking Sequence	P_{max} [kN]	ϵ_{max} [%]
$[0]_8$	75.48170	1.617
$[0/90/90/0]_s$	51.69043	1.274
$[90/0/0/90]_s$	29.92065	0.916
$[0_2/\text{-}45_2/45_2/90_2]_s$	77.394	1.696

Table 3: Yielding point test results

5. Optical Measurements

For TSA measurements, a **FLIR** X6580sc infrared camera with a InSb (Indium Antimonide) sensor, capable of an infrared image resolution of 640×512 pixels, 355Hz maximum frame rate (at the maximum resolution) and with a thermal sensitivity < 25 mK, was used.

Processing of the acquired results thermal images were done recurring to the **DisplayImg 6** software. Three main parameters were extracted

- **Temperature Amplitude:** Corresponds to the average temperature amplitude due to thermoelastic effects;
- **Absolute Temperature:** Corresponds to the average absolute temperature;
- **Phase Angle:** The angle correspondent to the phase difference between the applied load signal and the temperature signal read by the camera;

The phase angle value for the TSA measurements corresponds to the phase shift between the measured thermal wave and the reference signal, given by the Instron machine through a Lock-In hardware cable. For adiabatic conditions this value should be equal to zero.

Calibration of the camera (figure 2), image acquisition and further post processing was done, through the **ARAMIS Professional** software. Calibration for 2D DIC system yielded a calibration deviation of 0.018 pixels and a scale deviation of 0.02 mm.

Output parameters from the DIC measurements consisted in the full-field strain change in the loading and transverse direction, $\Delta\epsilon_x$ and $\Delta\epsilon_y$.

6. Preliminary Test

Certain test parameters had to be computed in order to obtain accurate TSA measurements.

6.1. Emissivity Test

One of the parameters required to be input in the **DisplayImg 6** was the emissivity of the surface under evaluation. Joint employment of 2D-DIC and TSA require the structure to be painted with a random gray intensity distribution. Quantification of the speckle pattern and the CFRP surface layer emissivity will provide a more consistent value within the ones available in the literature. A

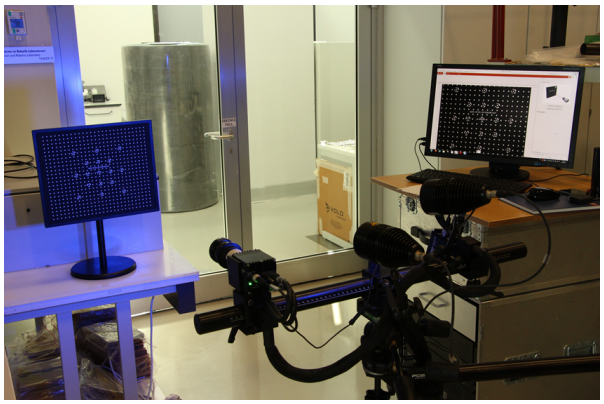

Figure 2: 2D DIC system Calibration

unidirectional UD sample, with 1.5mm thickness, vertically divided into areas containing a speckle pattern, an Epoxy layer, a 3M black tape and an aluminium foil piece was placed inside a climate chamber at a temperature of 55°C and values of the software's emissivity parameter were changed. By positioning the FLIR camera, with a 50 mm lens attached to it, at a sufficient distance to avoid heat gradients in the lens' surface optimal values for the emissivity of the Epoxy layer and the speckle pattern were computed as 0.95 and 0.97, respectively.

6.2. Frequency Test

Obtaining adiabatic conditions during TSA measurements requires the material to be dynamically loaded with a frequency enough to prevent heat conduction within it's internal structure. In order to determine the appropriate frequency to use for the TSA measurements, a unidirectional sample, UD0, with 2.23 mm thickness was tested in an Instron 8801 servo-hydraulic machine and the temperature emission was measured by positioning the FLIR camera at a distance of 73 cm from the sample. For this test, the values of 5, 8, 10, 12, 15, 18 and 20 Hz were used for evaluating the temperature emission of the sample and the results are expressed in figure 3, where the vertical axis corresponds to the ratio between the average temperature amplitude of the sample and the average absolute temperature value, $\Delta T/T_0$. For frequencies higher than 12 Hz, vibration effects became a major concern due to the errors it induced in the measurements. This issue was solved by placing a foam underneath the camera's tripod legs.

Evaluation of the results obtained in figure 3 implies that there is a slight increase in the temperature response for carbon fiber polymers with the frequency. These results seem to be consistent with the ones achieved in previous quantitative TSA measurements[11, 12]. Therefore, 20 Hz was assumed to be the conditions which provided the closest adiabatic conditions possible.

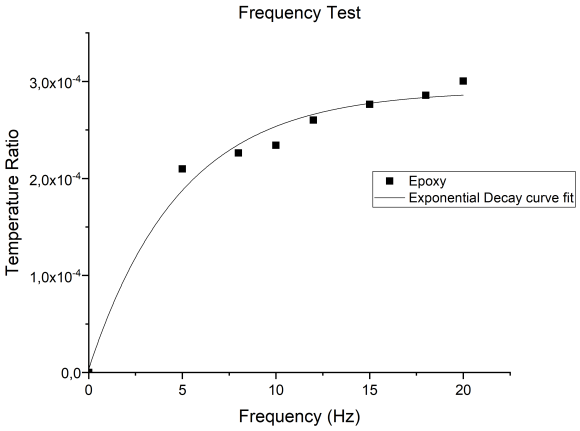

Figure 3: Frequency Test

6.3. Speckle Pattern Temperature Amplification

The speckle pattern was incorporated in the measurements to simulate more accurately the conditions for the application of this work to real structures. Therefore, it is important to evaluate the influence of the speckle pattern in the temperature measurements. As it was demonstrated in section 6.1, an increase emissivity value is obtained with the speckle pattern. Previous tests involving thermoelastic effect measurements for metals required the painting of these materials with a uniform surface coating, in order to increase its emissivity. These layers proved to induce temperature amplifications of 20% and phase reductions at the current working frequencies. Wang et al.[13], also employed DIC and TSA measurements to address complex motion compensation techniques and derived an almost non-existent influence of the speckle pattern in the thermoelastic response of the material. In order to obtain a more consensual value for the amplification of the thermoelastic signal, an unidirectional sample was tested and proved to provide a signal increase of 3% in the temperature emission between non painted and painted samples.

7. Experimental Procedure

Standard TSA measurements involve the dynamic testing of the material at high frequencies so that adiabatic conditions are attained. Incorporation of DIC measurements in this type of test does not provide the solution to the problem at hand since the CCD sensor is not able to provide sufficiently high frame rates for clear image acquisition.

Nevertheless, since TSA is applied for elastic deformations, where all deformations are reversible, a quasi-static tensile test with deformation measurements performed between the same load intervals as the dynamic test will give the same deformation, and therefore, equivalent strain changes.

To ensure the two load tests' analysis are performed within the same loading limits, two 75Ω analog coaxial cable were connected, from the Instron 8853 Servo-hydraulic machine, to the DIC system and an analog signal was sent once loading reach the minimum and maximum limits of the dynamic test.

Providing the aforementioned assumptions are valid, a correlation between the two performed tests can be stipulated. This way, two types of tests were performed under load control, so that no overestimation of the material's elasticity occurred.

- Dynamic tension-tension test at 20Hz frequency, between the loads P_{min} and P_{max} of table 4, performed in an Instron 8801, with an IR image acquisition at a frame rate of 355 Hz;

- Quasi-static tensile test at a rate of 3kN/min, for a maximum load correspondent to 15% of the yield point, performed in an Instron 8853, with an image acquisition at a frame rate of 0.5Hz;

For the dynamic test, a tension-tension test should be performed for TSA measurements. If the minimum load for this test is equal to 0, inaccuracy of the servo-hydraulic machines could make the material enter compression loads. Therefore, the minimum load was set according to the data in table 4.

Stacking Sequence	Load Threshold [kN]
$[0]_8$	2-12.5
$[0/90/90/0]_s$	2-7.75
$[90/0/0/90]_s$	1-4.49
$[0_2/\text{-}45_2/45_2/90_2]_s$	2-11.25

Table 4: Laminate's load Threshold

8. Data extraction and interpolation

Output data is stored in a pixel-wise manner. However, depending upon cameras' resolutions, the same geometrical location of a material point in the specimen can be represented by two distinct sets of pixels. Therefore, data comparison is only made possible if one interpolates both final datasets into a common mesh with a reduced number of structured grid points, here defined as background mesh.

The function value at point x represented in the background mesh, ξ, can be expressed as [14],

$$f(\boldsymbol{x}) = \sum_{i=1}^{N} w_i \phi\Big(||\boldsymbol{x} - \boldsymbol{\xi}_i||\Big) \tag{14}$$

where w_i is the weight constant, $\boldsymbol{x}$ is the bi-dimensional space defined as the input space, ξ

corresponds to the reference points of the background mesh and ϕ is denoted as a Kernel function. In this work, the Kernel function was given by a negative exponential function, yielding

$$\phi\Big(||\boldsymbol{x}-\boldsymbol{\xi}_i||\Big) = exp\Big(-||\boldsymbol{x}-\boldsymbol{\xi}_i||^2\Big) \quad (15)$$

This formulation allows attaining a maximum correspondence when the points of the two meshes match ($\boldsymbol{x}$ and $\boldsymbol{\xi}$) and diminuish exponentially with the increasing distance from the calculation point.

9. Results and Discussion

After interpolating the outputs from both cameras into the reference mesh, through an RBF based interpolation, the strain values from DIC measurements were converted into temperature ratio values, $\Delta T/T_0$, through the replacement of local strain value, $\Delta\epsilon_x$ and $\Delta\epsilon_y$. The remaining parameters were replaced with the values summarized in table 2 in the thermoelastic equations of the described models. These local temperature ratio values constituted the theoretical values for these measurements. Summary of these steps is presented in figure 4.

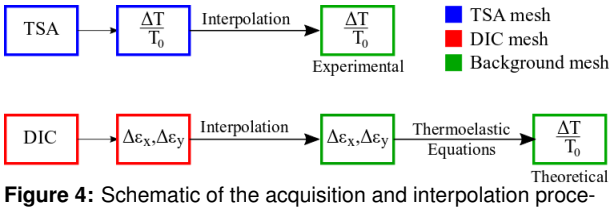

Figure 4: Schematic of the acquisition and interpolation procedure

Afterwards, the theoretical temperature ratio was compared with the one obtained through usage of the thermal camera. The error, for each model was computed following equation 16.

$$e(\%) = \frac{|(\Delta T/T_0)_{DIC} - (\Delta T/T_0)_{TSA}|}{(\Delta T/T_0)_{DIC}} \times 100 \quad (16)$$

The point-wise error of the thermoelastic ratio for each model was computed, and the local characterization of the thermoelastic behaviour was assigned to the model which allowed the minimum error. Thus, two maps containing the model correspondent to each pixel and the respective minimum error were obtained, illustrated in figures 5 and 6.

Analysis of figure 5, confirms the limitations of the global calibration of the thermoelastic signal, since considerable locations of the sample have different models assigned. These models will differ from the one foreseen in the gage length's center, where strain gauges would be attached. Furthermore, one of the referred consequences of the conventional methodology for quantitative TSA measurements is the under/overestimation of the material's

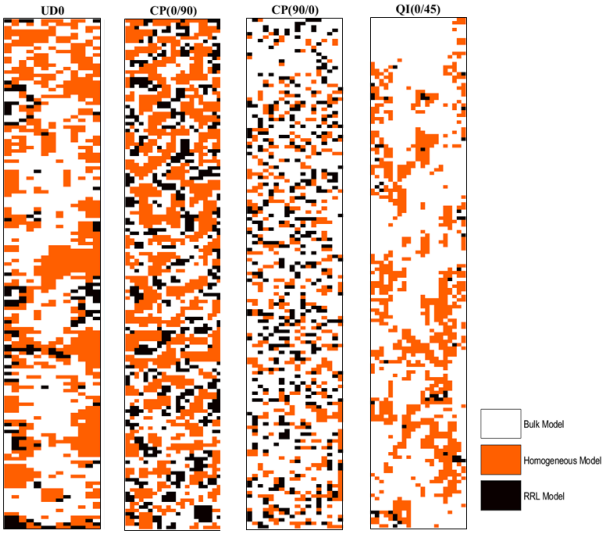

Figure 5: Local thermoelastic signal calibration

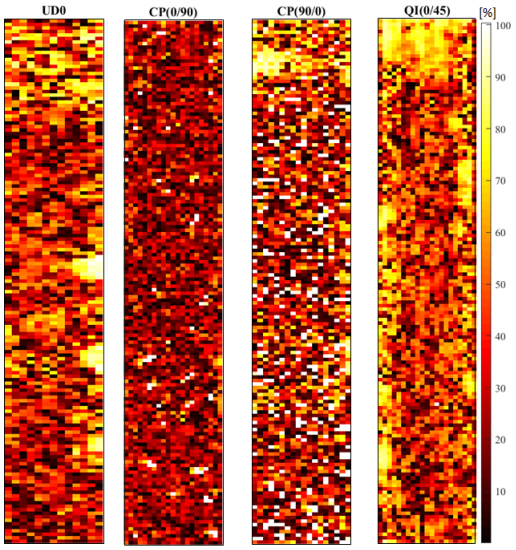

Figure 6: Local minimum error map

mechanical deformation. Further analysis of the obtained results allow the average error for all the stacking sequences to be computed, illustrated in table 5.

For the UD0 sample, the distribution of the thermoelastic models reveals a predominance of the bulk model, covering around 53.90% of the sample's area. Accuracy of the results are reinforced by the averaged phase angle of 5.1976º during TSA measurements, meaning adiabatic conditions appear to have been attained. Nonetheless, 39.24% of the sample's area has a thermoelastic response closer to the homogeneous model. Similar TSA works with low loading frequencies[15] have concluded that the homogeneous model better represents the thermoelastic behaviour due to the influence of inner plies in the surface's thermal response. However, in the authors perspective, since the homogeneous model's mathematical formula-

tion relies in the assumption of isentropic deformation processes, this argument seems not to be valid. Finally, only 6.87% of the sample's area has a thermoelastic response closer to the resin-rich layer model, which is in agreement with the conclusions arrived by Pitarresi and Galietti[16].

Although the temperature signal from the resin is reduced, an increase of 3.13% was observed between the average experimental temperature ratio obtained through the bulk model. On the other hand, if the homogeneous model would have been used to characterize the global thermoelastic behaviour of the material, an average increase of 8.74% would have occurred. A justification for no apparent temperature ratio difference between models might lay in the low order of magnitude of the applied load. An increase in the maximum load of the test could enhance this difference. Another factor that could justify the reduced differences between the two models is the quality of the laminate and the lack of defects in the material, which leads to a higher homogenization of the material.

Attending on the CP laminates, there are considerable locations for which the homogeneous model seems to provide lower correlation errors. Considering the theoretical background behind this model, the thermoelastic response reflects a high influence of the laminate's properties. This fact has been pointed out in cross ply laminates due to the high mismatch in thermo-mechanical properties between 0° and 90° plies. This translates in the generation of opposing magnitude stress fields, thus increasing the through thickness stress gradient and preventing retention of the heat generated due to the thermoelastic effect in the surface ply. This assumption is reinforced by increase of the average phase angle. For the CP(0/90) and CP(90/0) samples, phase angles of 15° and 23° were respectively attained.

For the QI(0/45) sample, the increase in the number of plies, in relation to other configurations (from 8 to 16 layers), appears to have led to an homogenization of the material's thermoelastic response, since only the bulk and homogeneous models present a considerable area percentage, 70.89 % and 27.55%, respectively. This could be resultant from stacking two plies with the same orientation near the surface observed by the IR detector, thus reducing any mismatch between properties of different orientation plies. An average 7.39% increase on the temperature ratio is obtained between the areas characterized by the homogeneous and the bulk model. The RRL model, accounting for only 1.56% of the whole area, gives a thermoelastic response 2.66% lower than the bulk model.

Even though this work appears to provide a better approach for evaluating the material's stress state, inspection of table 5 reveals a high percentage for the average minimum error for every stacking sequence. Several sources of error might be referenced, whose combination might lead to considerable errors.

- The measuring distance between the IR camera and the specimen together with the lens magnification employed in the camera makes any small vibrations in system to be amplified in the detector's signal;
- Vibrations in the camera which induced erroneous measurements;
- Correlation between the two techniques was done between different load stages;
- The small changes in temperature due to the thermoelastic effect, around 10^1 mK, make the accuracy of the results highly sensitive to small disturbances during the TSA measurements.

Laminate Code	Average Error (%)
UD0	31.8011
CP(0/90)	28.1484
CP(90/0)	60.2925
QI(0/45)	41.7037

Table 5: Minimum error for each stacking sequence

Assuming the influence of experimental errors in the TSA and DIC's output does not compromise the accuracy of the calibration process, another hypothesis should be drawn to explain the source of the inaccuracy of the previous results.

The following proposal has been previously referred by Pitarresi and Galietti[16]. Many engineering materials have a positive coefficient of thermal expansion, α, meaning an extension, in a certain direction, occurs once temperature increases. In the case of carbon fibers, this value is negative at room temperature. On the other hand, the epoxy resin has a positive CTE value at the same temperature conditions. This mismatch between the fiber and matrix's CTE generates a material whose CTE is highly sensitive to fiber/matrix volume ratios.

Therefore, switching from a global coefficient of thermal expansion, for the outer lamina, to a local value, which takes into account fiber/matrix volume ratio fluctuations will give a more accurate result for the material's thermoelastic behaviour.

10. Local distribution of CTE

For increasing the sample data of the newly develop approach, more values for CTE in the longitudinal direction were obtained through TMA tests,

according to ASTM E831 standard. This will aid the identification of the CTE values that should be included in the set range.

The local-based thermoelastic assignment and correspondent error, obtained by ranging α_1 values from the minimum and maximum, obtained through TMA tests and summarised in table 6, are illustrated in figures 7 and 8.

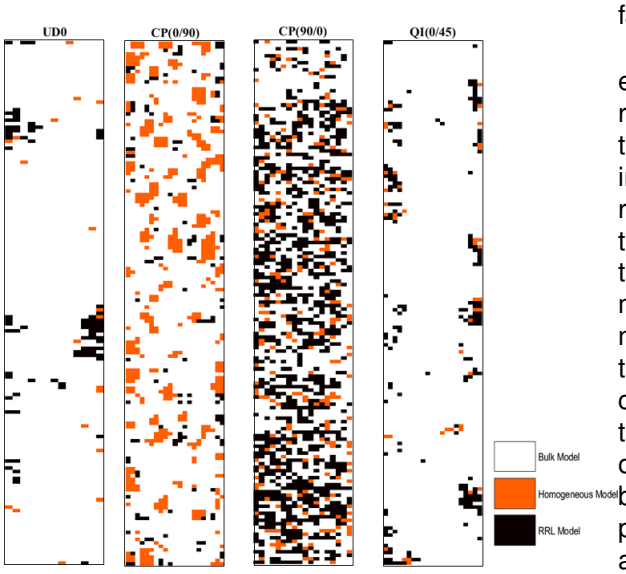

Figure 7: Local thermoelastic signal calibration with CTE distribution

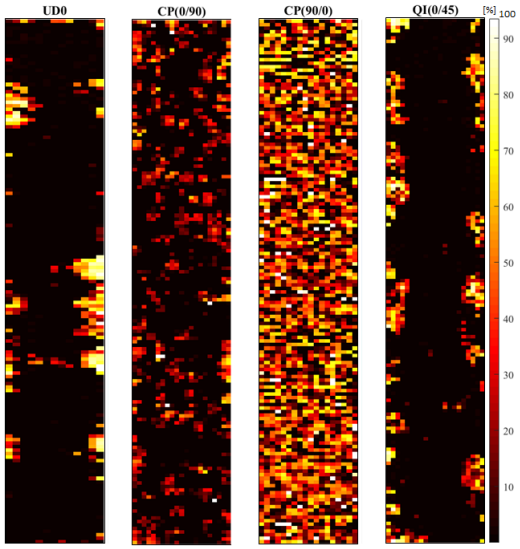

Figure 8: Local minimum error map with CTE distribution

Comparison between the local distribution of the thermoelastic models, figures 5 and 7, clearly show the replacement of the homogeneous model with the bulk model. This way, locations which appear to have a thermoelastic response with high influence from the laminate, instead were not taking into account fiber/ratio volume ratio variations. This effect is particularly significant in the unidirectional sample, where the percentage of locations under the homogeneous model decreased from 39.18% to 0.938%.

The results for the cross ply with the surface ply oriented at 90° are consistent with the literature review, since for this laminate there is an increase on the thermoelastic response from the surface layer. Percentage of the resin rich layer model increased from 4.35% to 35.94%, with the change in the surface ply orientation.

Evaluation the average error's reduction between each sample reveals that the laminate whose error reduction occurred in a lower percentage was the Cross Ply sample with surface ply at 90°, while in the sample with a surface layer at 0° the error decrease was 72.33%, in the CP(90/0) sample the error decreased 58.03%. This fact, in addition to the presence of locations with high error in the middle of the sample, leads to the conclusion that non-adiabatic effects might have been present in the sample. This could have been originated in cracks, voids or heat generation due to friction of the plies. Nonetheless, the possibility that some overload might have occurred in the sample cannot be dismissed. The same consideration should apply to the CP(0/90) sample due to the existence of a high number of points, within the laminate, which present high error value.

Reduction of, 82.05% and 83.75% of the average minimum error were obtained, respectively, for the UD0 and QI(0/45) samples. The high error decrease in the unidirectional and quasi-isotropic sample yields a particular significance due to the high application of these laminates in aerospace structures.

Laminate Code	Average Error (%)
UD0	5.7098
CP(0/90)	7.7893
CP(90/0)	34.9963
QI(0/45)	6.7745

Table 6: Minimum error for each stacking sequence

The aforementioned evaluation of the results obtained through a local CTE distribution might not fully provide an accurate assessment of the errors, given that the real value for the CTE in each point is unknown. Therefore, the true validation of this last proposal can only be confirmed by evaluating the true point-wise CTE value, in the sample.

Complementing this approach, the values of other variables, namely E_1, could also present some variation, since only the average value was used from the values obtained through the various tests. The variability of α_x and α_y can also be confirmed by the value difference obtained in the TMA analysis for the CP(0/90) and CP(90/0) samples, since these two values should be equal, given the lami-

nate's configuration. However, increasing the variability and combinations of parameters in the simulation will harshly increase the computational cost of such method.

11. Conclusions

With this work, a new methodology for quantitative thermoelastic measurements for carbon fiber reinforced materials was developed in order to take into account the material's heterogeneity and the full-field characteristics of Thermoelastic Stress Analysis, by employing Digital Image Correlation instead of Strain Gauges. Moreover the previously discussed local behaviour of the Coefficient of Thermal Expansion was addressed and an improvement of the results was obtained.

12. Acknowledgements

The financial and infrastructural support provided by Sabanci University - Integrated Manufacturing Technologies Research and Application center, Sabanci University - Kordsa Composite Technologies Center of Excellence, and the Individual Research Funding is greatly acknowledged.

References

[1] C. Soutis. 1 - introduction: Engineering requirements for aerospace composite materials. In *Polymer Composites in the Aerospace Industry*, pages 1 – 18. Woodhead Publishing, 2015.

[2] Christos Kassapoglou. *Design and Analysis of Composite Structures With Application to Aerospace Structures*. Wiley, 2 edition, 2013.

[3] K. Ramesh. Structural health monitoring – its association and use. In *New Trends in Structural Health Monitoring*, pages 1–79. Springer, Boston, MA, 2013.

[4] Richard J. Greene. *Thermoelastic Stress Analysis*, chapter Springer Handbook of Experimental Mechanics. Springer US, 2008.

[5] M.A. Sutton, J.J. Orteu, and H. Schreier. *Image Correlation for Shape, Motion and Deformation Measurements: Basic Concepts,Theory and Applications*. Springer Publishing Company, Incorporated, 1st edition, 2009.

[6] GOM. Digital image correlation and strain computation basics. Technical report, GOM, 2016.

[7] B. Pan, K. Quian, H. Xie, and A. Asundi. Two-dimensional digital image correlation for in-plane displacement and strain measurement: a review. *Measurement Science and Technology*, 20(6), 2009.

[8] W. Thomson. Ii.- on the thermoelastic, thermomagnetic, and pyroelectric properties of matter. *The London, Edinburgh, and Dublin Philosophical Magazine and Journal of Science*, 5(28):4–27, 1878.

[9] R. T. Potter. Stress Analysis In Laminated Fibre Composites By Thermoelastic Emission. *Stress Analysis by Thermoelastic Techniques*, 0731(April 1987):110, 1987.

[10] G. Pitarresi, M.S. Found, and E.A. Patterson. An investigation of the influence of macroscopic heterogeneity on the thermoelastic response of fibre reinforced plastics. *Composites Science and Technology*, 65(2):269 – 280, 2005.

[11] A.K. Wong. A non-adiabatic thermoelastic theory for composite laminates. *Journal of Physics and Chemistry of Solids*, 52(3):483 – 494, 1991.

[12] C.E. Bakis and K.L. Reifsnider. The adiabatic thermoelastic effect in laminated fiber composites. *Journal of Composite Materials*, 25(7):809–830, 1991.

[13] R. K. Fruehmann W. Wang and J. M. Dulieu-Barton. Application of digital image correlation to address complex motions in thermoelastic stress analysis.

[14] V. Skala. A practical use of radial basis functions interpolation and approximation. 37:137–145, 01 2016.

[15] D. Crump and J. Dulieu-Barton. Performance assessment of aerospace sandwich secondary structure panels using thermoelastic stress analysis. *Plastics, Rubber and Composites*, 39:137–147, 06 2010.

[16] G. Pitarresi and U. Galietti. A quantitative analysis of the thermoelastic effect in cfrp composite materials. *Strain*, 46(5):446–459, 2010.